Applied Surface Science Advances 25 (2025) 100668

Contents lists available at ScienceDirect

Applied Surface Science Advances

journal homepage: www.sciencedirect.com/journal/applied-surface-science-advances

Full Length Article

The effect of annealing on the structural, optical, electrical and photoelectric properties of ZnO/NiO heterostructures

M. Yermakov [a,*], R. Pshenychnyi [a], A. Opanasyuk [a], Yu. Gnatenko [b], P. Bukivskij [b], A. Bukivskii [b], O. Klymov [c], V. Muñoz-Sanjosé [c], R. Gamernyk [d]

[a] Sumy State University, Kharkivska str., 116, Sumy UA-40007, Ukraine
[b] Institute of Physics of National Academy of Sciences of Ukraine, 46 Nauky Pr., Kyiv 03028, Ukraine
[c] Department of Applied Physics and Electromagnetism, Universitat de València, C/Dr. Moliner 50, Burjassot 46100, Spain
[d] Ivan Franko National University of Lviv, 8 Kyrylo and Mefodiy Str., Lviv 79005, Ukraine

ARTICLE INFO

Keywords:
n-ZnO/p-NiO heterostructures
Spray pyrolysis
Annealing effects
Diffraction analysis
Optical properties
Rectifying-electrical properties

ABSTRACT

In this study, *n*-ZnO/*p*-NiO heterostructures on glass substrates with an indium tin oxide (ITO) covering were obtained by using the spray pyrolysis methodology. In order to act on the structural and local compositional defects, the samples were annealed under vacuum in the temperature range of $T_a = (300 – 500)$ °C in steps of $\Delta T = 50$ °C. X-ray diffraction results indicate the presence of only the hexagonal ZnO and cubic NiO phases in the studied samples, which was confirmed by Raman spectroscopy. Low-temperature photoluminescence (PL), as well as absorption and photoconductivity, were studied to establish the optical properties, the nature of electronic optical transitions, the energy level position of the different defects present in the samples, and the effect of temperature annealing on these properties The band gap of the compounds was determined using the Tauc approximation and the first derivative of the absorption coefficient. Likewise, the current-voltage characteristics of the *n*-ZnO/*p*-NiO heterostructures and their diode character, were analyzed.

1. Introduction

Rapid technological advances drive the ever-increasing demand for electronic devices with improved performance and new functionalities. Increasing the efficiency of devices requires the search for new semiconductor materials and heterostructures which could be available for these devices. In this frame, in a recent paper [1] we have studied the structural and electrical properties of the *n*-ZnO/*p*-NiO heterostructure obtained by the scalable spray pyrolysis technique because the opportunities of this heterostructure to develop portable ultraviolet detectors, transistors, and gas sensors transparent in visible light SC, etc. [2–6]. It should be noted that the materials that make up this heterostructure are cheap, environmentally safe, and can be obtained using many technologically simple methods [5–8]. As previously discussed [1] today, ZnO is one of the most widely used transparent oxides. This is due to its unique electrical, chemical, physical, and optical properties, as well as chemical, radiation, and thermal stability in the atmosphere and non-toxicity [9]. Zinc oxide shows *n*-type conductivity, and it has a direct band gap ($E_g = 3.37$ eV) and a high exciton binding energy, as well as a high carrier mobility, and it is considered as an alternative to traditional materials for transparent conductive layers as ITO and FTO when used in many electronic devices [6]. In addition, ZnO can be applied as an active layer of gas sensors, photodetectors, light emitting lasers, and LEDs, as a catalyst, in SCs as an anti-reflective coating or window layer, i.e., it is a multifunctional material [10].

On another side, nickel oxide is considered a promising material for the fabrication of oxide heterostructure, as it is one of the few chemically stable wide-band compounds ($E_g = (3.6–4.0)$ eV) with *p*-type conductivity [11]. NiO has a cubic crystal lattice structure and can offer high crystallinity [12]. In addition, it has many valuable properties, such as low toxicity, prevalence of components in the earth's crust, high chemical stability, simple synthesis, significant work function of ~5.4 eV), and deep valence band maxima, $V_{BM} \sim 5.4$ eV [13,14]. Nickel oxide can be applied to produce transparent, highly conductive layers with hole conduction in the development of photocatalysts, battery cathodes, electrochemical devices, and solar heat absorbers [15]. Thus, NiO is now an attractive electronic material with great potential for use in sensors and optoelectronic devices.

* Corresponding author.
E-mail address: m.yermakov@ekt.sumdu.edu.ua (M. Yermakov).

https://doi.org/10.1016/j.apsadv.2024.100668
Received 30 August 2024; Received in revised form 19 November 2024; Accepted 23 November 2024
Available online 28 November 2024

In this paper, the study of the structural characteristics, as well as the optical properties and the analysis of the rectifying electrical behavior of the *p*-NiO/*n*-ZnO heterostructure, obtained by the spray pyrolysis method on Glass/ITO substrates are presented, and the effect on those properties of the annealing in the range of (300–500) °C under vacuum is analyzed.

2. Materials and methods

Thin ZnO and NiO layers were obtained by spraying molecular solutions (spray pyrolysis) onto heated ITO substrates. Aqueous solutions of zinc and nickel acetates $Zn(CH_3COO)_2{\cdot}2H_2O$ (0.5 mol/l) and $Ni(CH_3COO)_2{\cdot}4H_2O$ (0.5 mol/l) were sprayed sequentially. Likewise, to obtain ZnO:In(1%) layers, solutions of zinc acetate and indium (III) chloride ($InCl_3{\cdot}3H_2O$, 0.25 mol/l) were mixed in the required ratio. More details of this scalable process can be found in [1]

The obtained multilayer structures were annealed in a vacuum environment at different temperatures $T_a = 300$, 350, 400, 450, and 500 °C for 60 minutes to study the effect of the annealing temperature on the optical properties and rectifying the electrical behavior of the heterojunction. The samples were allowed to cool naturally to room temperature to prevent or reduce thermal stress cracking of the layers. One of the samples was not annealed for comparison.

The thickness of films in multilayer structures was determined from cross-sectional SEM measurements. For this, samples were broken in half. Annealing led to a slight decrease in the thickness of the films (about 10 %), which is due to the removal of residual moisture in the layers.

A DRON 4–07 X-ray diffractometer was used to determine the structural properties of oxide films. The analysis was carried out under the Ni-filtered K_α-radiation of a copper anode. Using the Bragg-Brentano X-ray configuration, the diffractograms were taken in a continuous recording mode (speed - 16 °/min, step 0.1 °) in the range of 2θ angles from 20° to 80°, where 2θ is the Bragg angle. The obtained results were processed using the OriginLab software [16].

The obtained diffractograms were normalized to the intensity of the (111) peak of the NiO cubic phase. The phase analysis was performed by comparing the diffraction angles of the analyzed samples with the diffraction angles according to JCPDS table data (NiO - №00–047–1049, ZnO - №36–1451).

The texture quality of the layers of the obtained structure was evaluated according to the Harris method [17]. The polar density was calculated according to the equation:

$$P_i = \frac{(I_i/I_{0i})}{\frac{1}{N}\sum_{i=1}^{N}(I_i/I_{0i})}, \quad (1)$$

where I_i and I_{0i} are the integral intensities of the *i*-th diffraction peak for the film sample and reference; *N* is the number of lines that are present on the diffractogram.

Having found the value of pole density, the orientation factor can be determined using the following equation:

$$f = \sqrt{\frac{1}{N}\sum_{i=1}^{N}(P_i - 1)^2}. \quad (2)$$

The method of determining other structural properties of samples is described in detail in [1].

The value of the unit cell volume of the materials was calculated using the equations: $V_{ZnO} = 0.866 \bullet a^2 \bullet c$, $V_{NiO} = a^3$ [18,19].

The morphology of the films was studied using a Hitachi S-4800 scanning electron microscope equipped with a Bruker X-ray detector for microanalysis of samples. The voltage in the microscope column was ~ 20 kV with a beam current of 10 mA. The thickness of the samples was determined by the cross-section image of the films. Image magnification of 100 K was used to examine the morphology of the surface and a 60K magnification was used for the cross-sectional determination of the samples.

Raman spectra of the films were analyzed in the frequency range (50 - 400) cm^{-1} using a Horiba MTB XPlora spectrometer at room temperature. A laser with a wavelength of $\lambda = 785$ nm and a power of 0.78 mW was used as an excitation light source. Raman studies were performed with three signal accumulations of 20 seconds each. At the same time, an Olympus BX-41 microscope with 50x magnification and a diffraction grating of 1200 lines per mm^{-1} was used.

A SILVER-Nova USB spectrometer was used to study the optical properties of the multilayer structures. The absorption spectra for the NiO layer were calculated by subtracting the spectra of ITO and the ZnO:In/ZnO double layer from the spectra of the entire structure. In addition to the absorption spectra of NiO, it was possible to detect the presence of a transition layer at the interface between the zinc oxide and nickel layers. To determine the band gap of materials, the Tauc approximation method [20] was used. E_g was also determined by the position of the maximum of the first derivative of the absorption coefficient (ACFD) of the material [21,22]. We also used a USB spectrometer MAYA 2000-pro (Ocean Optics) to study the photoluminescence (PL) spectra. Photoconductivity spectra were measured by equipment based on the KSVU-23 spectrometer.

The dark volt-ampere characteristics of heterostructure were measured according to the standard method [23] in the range of voltage change U = (-1.2) – (+1.2) V. The upper current-collecting contacts were made of Cu using the vacuum condensation method and variable masks. The contacts to the layers were applied directly after the deposition of the films to prevent their oxidation. The electrophysical properties of the obtained samples were measured in the air using an automatic system for measuring the dark I-V characteristics of a CS Ossila Solar Cell IV System. A schematic representation of the obtained multilayer structure with an *n*-ZnO/*p*-NiO heterostructure is shown in Fig. 1.

3. Results and discussions

3.1. Surface morphology

Fig. 2 shows electron microscopy images of the surface of NiO films in the Glass/ITO/ZnO:In/ZnO/NiO multilayer structure and the cross-sectional image of unannealed and vacuum-annealed samples at a temperature of 400 °C. The thickness of the ZnO (1% In), ZnO, and NiO layers were (178–149) nm, (291–304) nm, and (149–155) nm, respectively. Similar results with respect to the thicknesses were found for the

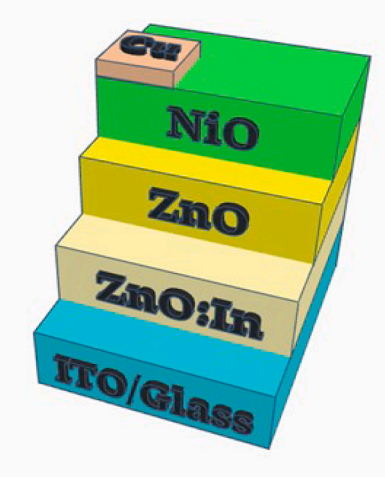

Fig. 1. Schematic representation of a Glass/ITO/ZnO:In/ZnO/NiO/Cu multilayer structure (a).

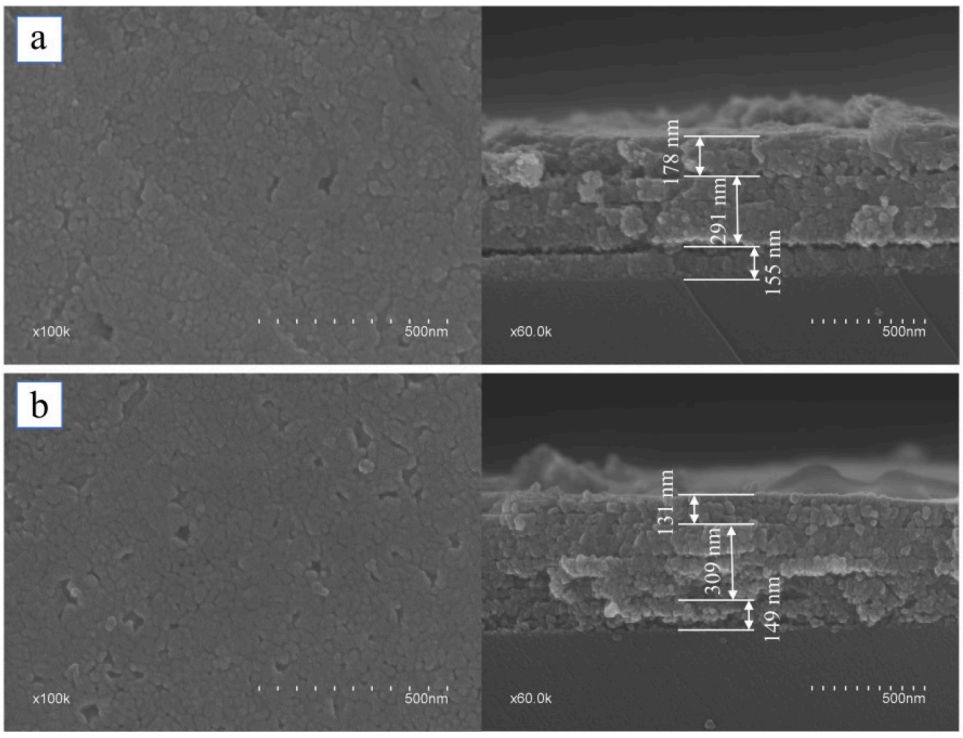

Fig. 2. Electron microscopy images of the surface and cross-sectional view of the Glass/ITO/ZnO:In/ZnO/NiO multilayer structure unannealed (a) and annealed at the temperature of 400 °C (b).

other annealing temperatures.

3.2. X-ray and Raman spectroscopy

In order to determine, undoubtably, the presence of the desired oxides into the structure, we performed an XRD and Raman spectroscopy analysis. Thus Fig. 3 presents diffractograms of the multilayer structures annealed at different temperatures. The peaks correspond to the reflections from crystallographic planes (111), (200), (220) and (222) of the cubic NiO phase and (100), (002), (101), (110), (103), (004) of the hexagonal ZnO phase. No other phases were detected in the materials of the multilayer structure. This means that their concentration, if any, did not exceed the resolution of the diffractometric method.

Fig. 4 a shows the results of the pole density calculations of the P_i films by constructing pole figures for the ZnO:In/ZnO layer. The figure shows that the double ZnO:In/ZnO layer has a well-degenerate growth texture [002], which does not change with the annealing temperature. The calculation of the orientation factor allowed us to determine the effect of temperature on texture quality. As can be seen from the inset in Fig. 4a, the texture quality of the ZnO:In/ZnO layer improved during annealing up to 450 °C and then decreased sharply. The maximum value of the orientation factor f is observed at T_a = 400 °C.

Fig. 4 b shows the dependence of the pole density P_i on the NiO layer. From the graphs, it was determined that the direction of growth of the texture of the NiO layer was a plane [111]. For the NiO layer, the annealing temperature does not affect the direction of the growth texture.

The results of the calculation of the orientation factor for the NiO layer are shown in the inset of Fig. 4 b. The texture quality of this layer improved at T_a = 300 °C and then remained almost unchanged up to T_a = 450 °C. However, when T_a = 500 °C, a sharp increase in f occurs, which can be explained by the recrystallization processes in the NiO layer that occur at critical annealing temperatures.

Diffraction reflection peaks from the crystallographic planes (100) and (101) were chosen to calculate the lattice parameter a of ZnO, while (002) and (103) were used to calculate the lattice parameter c (Table 1). Thus, the incertitude in the calculation of these parameters using Eqs. (1) and (2) is reduced, since the contribution of the term containing the equations (c/a) is minimized [18,19]. The reflections from the (111) and (200) planes, which had the maximum intensity, were taken to determine the lattice parameters of NiO.

The values of the lattice parameter a of the unannealed sample ZnO ($a_{(100)}$ = 0.3252 nm, $a_{(101)}$ = 0.3243 nm). With an increase in the annealing temperature to 400 °C, this parameter first decreased ($a_{(100)}$ = 0.3241 nm) and then increased ($a_{(100)}$ = 0.3262 nm, T_a = 500 °C). At the same time, the parameter c varied in the range of $c_{(002)}$ = (0.5199–0.5223) nm and $c_{(103)}$ = (0.5199–0.5237) nm, with a reference value of c = 0.5213 nm. The dependence on $c - T_a$ was similar to that observed for parameter a. At the same time, the minimum lattice parameter of the ZnO layer ($c_{(002)}$ = 0.5196 nm) was observed not at 400 °C, but at 350 °C.

The volume of the unit cell of zinc oxide was determined based on the calculated lattice parameters. The calculation was carried out based on pairs of values $a_{(100)}$ and $c_{(002)}$, $c_{(103)}$. It was established that during the annealing of the ZnO layer, the volume of the unit cell of the material changes as a function of T_a, similar to the parameters a, c, and reaches the value of V_{unit} = 48.13·10^{-3} nm^3 at T_a = 500 °C.

The lattice parameter of the NiO films in the unannealed state were $a_{(111)}$ = 0.4187 nm and $a_{(200)}$ = 0.4186 nm. At the same time, the lattice parameters found for the (111) and (200) reflections were close to each other for all obtained samples. In the following, the results obtained for the (200) reflection are discussed, which lies at larger angles and therefore provides more accurate results. It has been shown that a hardly changes a during annealing at the temperature of 300 °C. However, at T_a = 350 °C, this value decreased, approaching the value characteristic of a stoichiometric material. A further increase in T_a to 400 °C led to a sharp increase in the lattice period of the material, which, however, practically stabilized at the level of $a_{(200)}$ = 0.4201 nm (T_a = (450–500) °C) at higher annealing temperatures. The course of the dependence of $V_{NiO} - T_a$ for the NiO layer is similar to the course of the dependence of a - T_a. Initially, a decrease in the volume of the unit cell of the material from V_{NiO} = 73.3 nm^3 to V_{NiO} = 73.1 nm^3 (T_a = 350 °C) is observed, and with

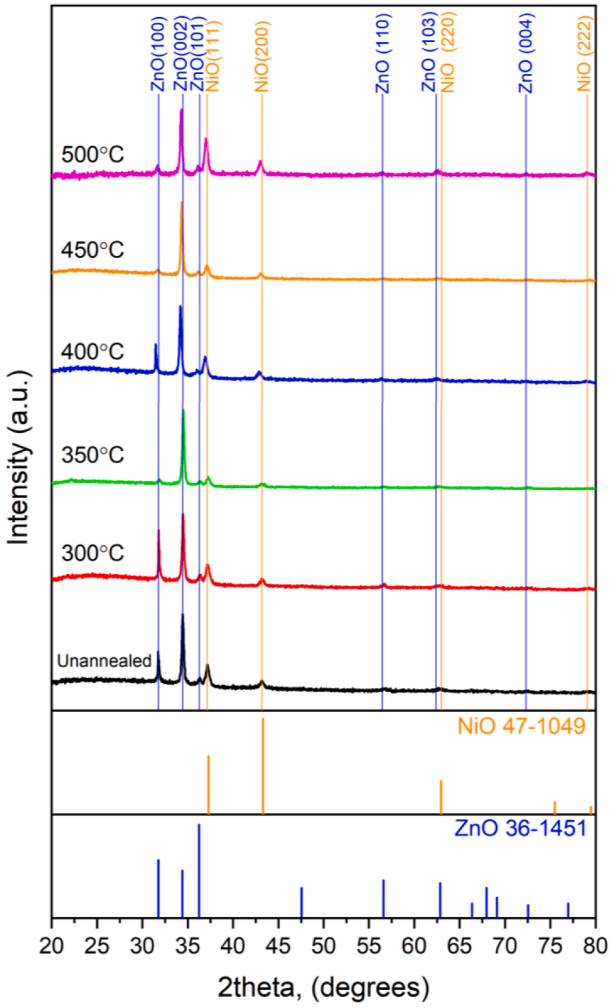

Fig. 3. Diffractograms of the unannealed and annealed at different temperatures Glass/ITO/ZnO:In/ZnO/NiO multilayer structures.

subsequent growth, the temperatures increased to V_{NiO} = 75.0 - 74.1 nm^3 (T_a = (400–500) °C). The analysis of the dependencies of the substructural characteristics of the layers of the *n*-ZnO/*p*-NiO heterostructure depending on the annealing temperature is described in our previous work [1].

On the other hand, Fig. 5 shows the Raman spectra of the Glass/ITO/ZnO:In/ZnO/NiO multilayer structure. The Raman spectra were measured in the frequency range from 50 cm^{-1} to 1200 cm^{-1}. The peaks present in these spectra are characteristic of both ZnO and NiO.

The peaks detected at frequencies (97–103) cm^{-1}, (366–391) cm^{-1}, (436–440) cm^{-1}, (567–578) cm^{-1}, (905–912) cm^{-1}, and (1125–1142) cm^{-1} belong to the ZnO layer. It is known [24] that these peaks belong to the phonon modes E2(Low)$_{ZnO}$, A1(TO)$_{ZnO}$, E2(High)$_{ZnO}$, A1(LO)$_{ZnO}$, A1(2TO)$_{ZnO}$, and A1(2LO)$_{ZnO}$, respectively. The E2(Low)$_{ZnO}$ and E2(High)$_{ZnO}$ modes are characteristic modes associated with zinc oxide. The E2(Low)$_{ZnO}$ and E2(High)$_{ZnO}$ modes are attributed to the vibrations of zinc cations and oxygen anions, respectively [25]. An intense E2(High)$_{ZnO}$ peak indicates a low concentration of intrinsic defects in the ZnO layer. The A1(TO)$_{ZnO}$ and A1(2TO)$_{ZnO}$ modes indicate the strength of the polar lattice bond [26]. The presence of A1(LO)$_{ZnO}$ and A1(2LO)$_{ZnO}$ peaks is usually due to the presence of oxygen vacancies [27].

Phonon and magnon modes in the Raman spectra of NiO layers overlap each other. Consequently, Lorentz functions were used to analyse the spectra. The first-order phonon modes of nickel oxide are in the range of (300–600) cm^{-1}, and the second-order phonon modes are in the (600–1200) cm^{-1} range [28].

The Lorentz functions decomposition method revealed the presence of peaks at the frequencies (477–508) cm^{-1}, (521–533) cm^{-1}, (795–799) cm^{-1} and (1019–1023) cm^{-1}. According to [29,30] these peaks belong to the phonon modes TO$_{NiO}$, LO$_{NiO}$, (LO+TO)$_{NiO}$, and 2LO$_{NiO}$, respectively.

Similar results were found for other annealing temperatures, and the presence of secondary peaks of other compounds was not detected in the Raman spectra, which confirms the results of the X-ray diffractometry.

3.3. Absorption spectra

Fig. 6 shows the absorption spectra of the Glass/ITO/ZnO:In/ZnO/NiO heterostructure. Curves 1–6 correspond to the unannealed sample and the samples annealed at temperatures of 300, 350, 400, 450, and 500 °C, respectively. The inset of Fig. 6 shows a scheme for measuring absorption spectra, according to which light passes through all layers of the structure. Thus, in this case, the total absorption of all layers of the heterostructure is measured. As can be seen from Fig. 6, the absorption spectrum of the Glass/ITO/ZnO:In/ZnO/NiO heterostructure mainly covers the ultraviolet part of the spectrum from 3.0 to 4.5 eV, since the components of the composition have large values of the band gaps (ZnO is about 3.4 eV [31] and NiO - from 3.6 to 4.0 eV [32–34]). The

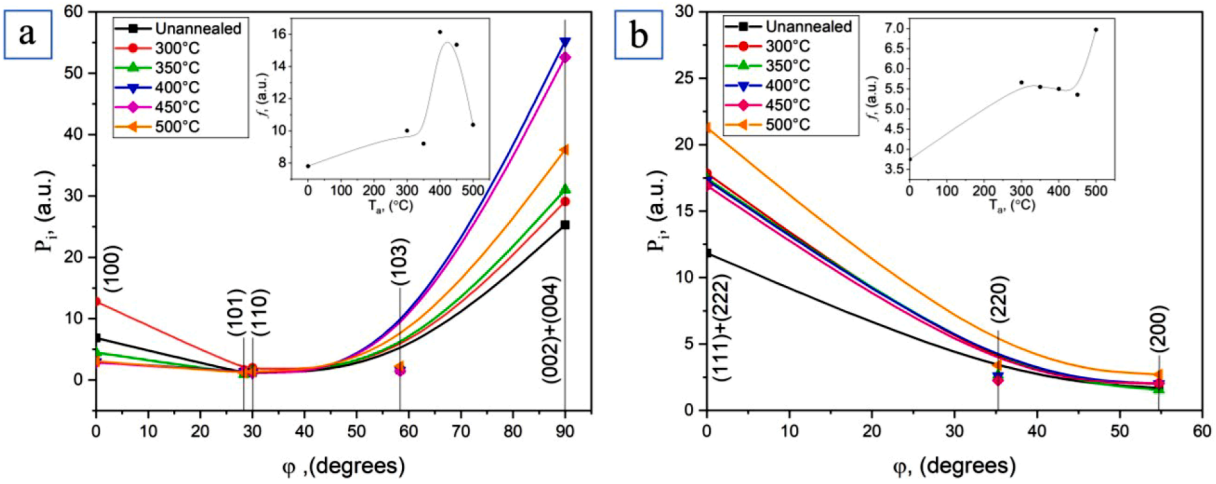

Fig. 4. Dependence of the pole density P_i on the angle φ between the texture axis and the normal to the reflection plane of the ZnO:In/ZnO (a) and NiO (b) layers on the annealing temperature. The insets show the dependence of the orientation factor f on the annealing temperature.

Table 1
Structural properties of unannealed and annealed ZnO and NiO layers for the *n*-ZnO/*p*-NiO heterostructure.

ZnO:In/ZnO layer							NiO layer			
T_a, °C	*a*, nm		*c*, nm		V_{unit} 10^3, nm^3		*a*, nm		V_{unit}, 10^3 nm^3	
	(100)	(101)	(002)	(103)	(100)(002)	(100)(103)	(002)	(101)	(002)	(101)
0	0.3252	0.3243	0.5202	0.5219	47.65	47.80	0.4187	0.4186	73.4	73.3
300	0.3248	0.3244	0.5199	0.5199	47.48	47.48	0.4188	0.4188	73.5	73.4
350	0.3239	0.3244	0.5196	0.5202	47.22	47.28	0.4175	0.4182	72.8	73.1
400	0.3241	0.3243	0.5211	0.5228	47.39	47.54	0.4213	0.4218	74.8	75.0
450	0.3246	0.3253	0.5217	0.5237	47.59	47.77	0.4193	0.4201	73.7	74.1
500	0.3262	0.3262	0.5223	0.5224	48.13	48.13	0.4204	0.4201	74.3	74.1
JCPDS a = 0.3253 nm, c = 0.5213 nm, V_{unit} =47.80·10^{-3} nm^3							JCPDS a = 0.4177 nm, V_{unit} =72.88·10^{-3} nm^3			

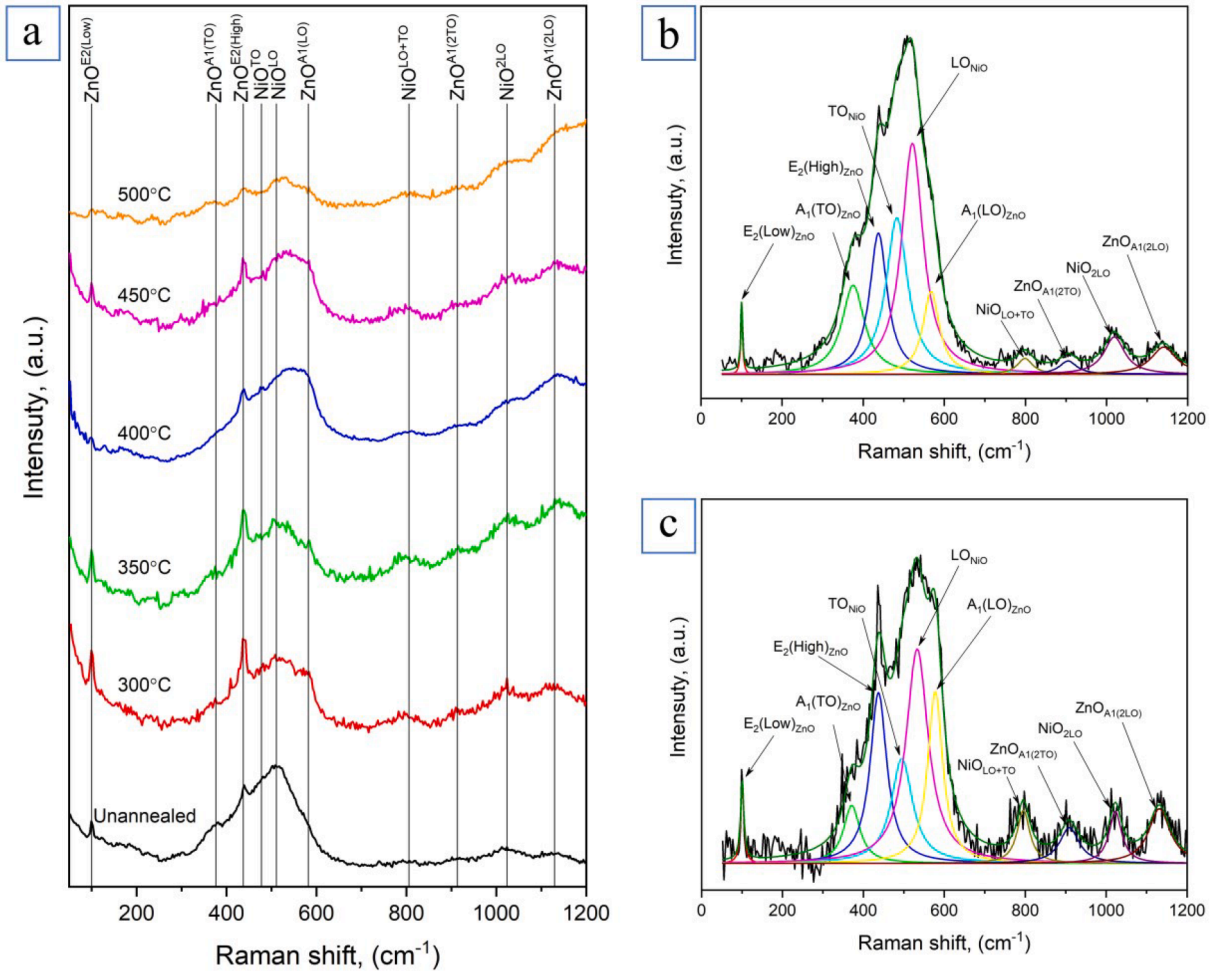

Fig. 5. Raman spectra from unannealed and annealed at different temperatures of Glass/ITO/ZnO:In/ZnO/NiO structures(a). Decomposition of the spectra by using Lorentz functions for unannealed (b) and annealed samples at 450 °C (c).

absorption of ZnO:In/ZnO layers in the range (3.2 – 3.5) eV is clearly visible. It should be noted that this absorption remains almost unchanged for the as-deposited sample and for samples annealed at temperatures $\leq$ 350 °C. With a further increase in the annealing temperature, the absorption of the zinc oxide layers decreases in the spectral region from 3.4 eV to 3.8 eV, where additional absorption, which is caused by the presence of a transition layer at the interface between the zinc and nickel oxide layers. Therefore, these changes in absorption are due to changes in absorption at the interface region. It should also be noted that the absorption background in the transparency region of the heterostructure is small since a steep absorption edge is clearly observed in the absorption spectra of zinc oxide films and is only weakly dependent on the annealing temperature, which indicates the optical quality of the investigated samples.

Fig. 7 a shows the absorption spectrum of the ZnO:In/ZnO double layer. The scheme of such measurements is presented in the inset, where it can be seen that the absorption spectrum was measured only for the ZnO:In/ZnO double layer. It should be noted that the spectral region of the measurement data corresponds to the transparency region of the ITO layer. Therefore, the presence of ITO does not affect the spectral dependence of absorption in this spectral region. It can be seen that the shape of the absorption edge and the absorption background in the

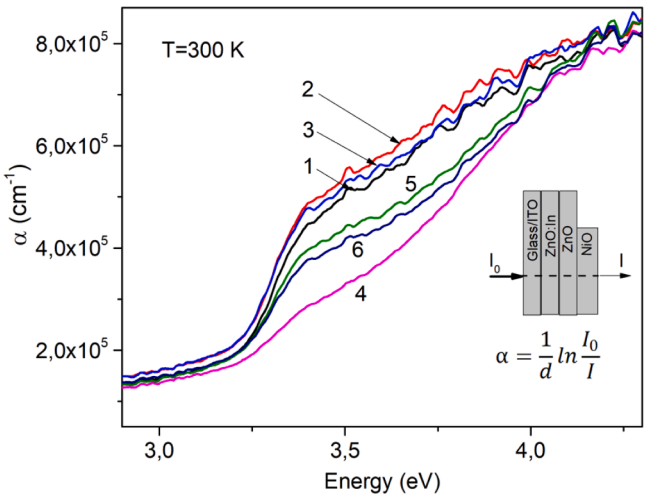

Fig. 6. Absorption spectra of the Glass/ITO/ZnO:In/ZnO/NiO heterostructure. Curves 1–6 correspond to the unannealed sample and samples annealed at temperatures of 300, 350, 400, 450, and 500 °C, respectively. The inset shows a scheme for measuring absorption spectra.

transparent region changes slightly in the samples annealed at temperatures not higher than $T_a = 450$ °C. While at a temperature of 500 °C, the steepness of the edge decreases, and the absorption background increases, which indicates a deterioration in the crystalline and optical quality of the zinc oxide layers. It should also be noted that in the case of samples annealed at temperatures $\leq$ 450 °C, the absorption edge shifts to the long-wavelength region of the spectrum, which may indicate an increase in the size of the nanocrystallites.

Fig. 7 b shows the absorption due to the superposition of the absorption edge of the NiO layer and the absorption associated with the interface between the zinc oxide and nickel layers. In this case, the intensity of incident light I_1 corresponds to the intensity of light passing through the Glass/ITO/ZnO:In/ZnO layer system. This light then passes through the interface between the ZnO and NiO layers and the NiO layer.

Based on the analysis of the shape of the absorption spectrum of zinc and nickel oxide layers using the Tauc approximation [35], as well as the ACFD method [22,34–38], estimations of the band gap of these layers and its dependence on the annealing temperature were carried out. Such approximations are shown in Fig. 8 in the case of the sample annealed at $T_a = 350$ °C.

Table 2 shows the values of the band gaps of the ZnO:In/ZnO and NiO layers of the as-deposited sample and the samples annealed at different temperatures, using the two methods mentioned above.

3.4. Photoluminescence spectra

Fig. 9 shows the low-temperature PL spectra (4.2 K) of the Glass/ITO/ZnO:In/ZnO/NiO multilayer structure of both the unannealed sample (a) and the samples annealed at 300 (b), 450 (c), and 500 °C (d). Curves 1–2 correspond to the spectra of the ZnO:In/ZnO and NiO layers, respectively. The scheme of such measurements is presented in the inset of Fig. 9 b. These spectra were obtained with a diode excitation at the wavelength of 274 nm, which allows excitation of both ZnO and NiO layers. Since the thickness of the different layers of the studied heterostructure was several hundred of nm, it allows measuring the PL spectra of both ZnO:In/ZnO and NiO layers when the upper NiO layer is excited.

As can be seen in Fig. 9 a (curve 1), the PL band at 379 nm (3.27 eV) is observed, which is caused by the exciton emission in ZnO [39]. Another two PL bands at 411 (3.02 eV) and 428 nm (2.90 eV) are due to the presence of defects like interstitial zinc, Zn_i [40]. At the same time, the existence of a band at 493 nm (2.51 eV) can be associated with the participation in the emission processes of donor-acceptor pairs with the presence of defects such as zinc vacancies [41,42]. In addition, a broad band at 745 nm is also observed in the PL spectrum, which can be associated with the presence of an O_{Zn}-type antisite defect in zinc oxide [43].

In the case of excitation of the NiO layer, additional PL bands at 529 (2.34 eV) and 880 nm (1.41 eV) are also observed. The first PL band is associated with the presence of nickel vacancies [44,45]. Besides, the emission at 493 nm may be associated with two - charged oxygen vacancies (O^{2-}) in NiO [46], i.e this PL band practically coincides with the band caused by donor-acceptor pairs in ZnO [41,42]. Similarly, the PL bands at 420 (2.95 eV) and 745 nm (1.66 eV) are observed in both ZnO:In/ZnO and NiO layers. It is obvious that the first band is double, that is, there are two components at 411 (3.02 eV) and 428 nm (2.90 eV) associated with defects such as oxygen vacancies.

In addition, as can be seen in Fig. 9 a (curve 2) there are two PL bands at 725 (1.71 eV) and 775 nm (1.60 eV) associated with the existence of oxygen vacancies in nickel oxide [47,48]. Thus, it can be concluded that the emission at 420 and 745 nm is caused by the presence of defects in both NiO and ZnO layers.

Fig. 9 b shows the PL spectra of ZnO:In/ZnO and NiO layers of the

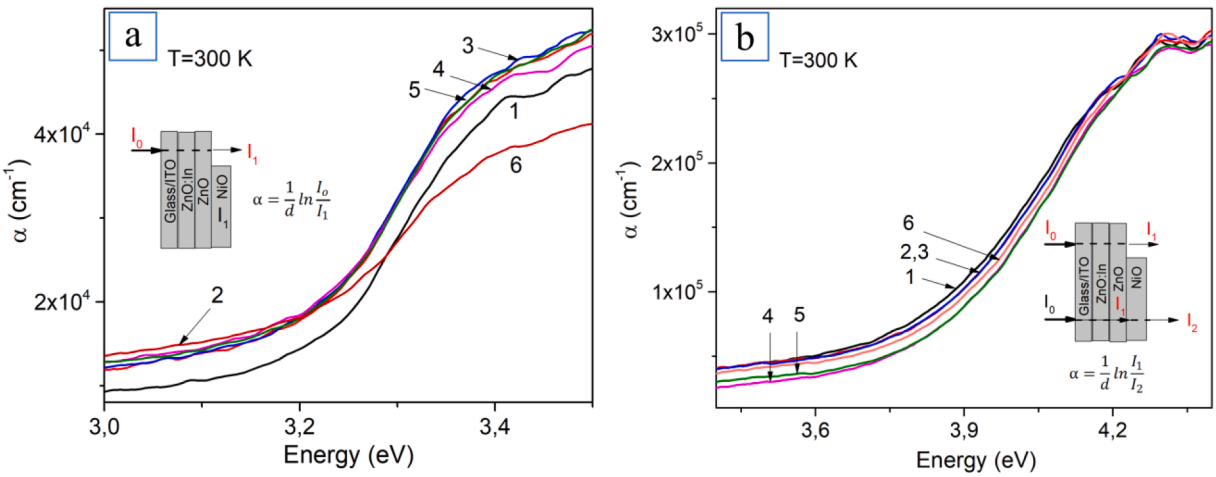

Fig. 7. Absorption spectra of the *n*-type ZnO:In/ZnO double layer of the ITO/ZnO:In/ZnO/NiO heterostructure annealed at different temperatures (a). Absorption spectra of the *p*-type NiO layer of the ITO/ZnO:In/ZnO/NiO heterostructure as well as the interface between zinc and nickel oxide layers of samples annealed at different temperatures (b). Curves 1–6 correspond to the unannealed sample and samples annealed at temperatures of 300, 350, 400, 450, and 500 °C, respectively (a, b). The insets show the measurement schemes of the absorption spectra.

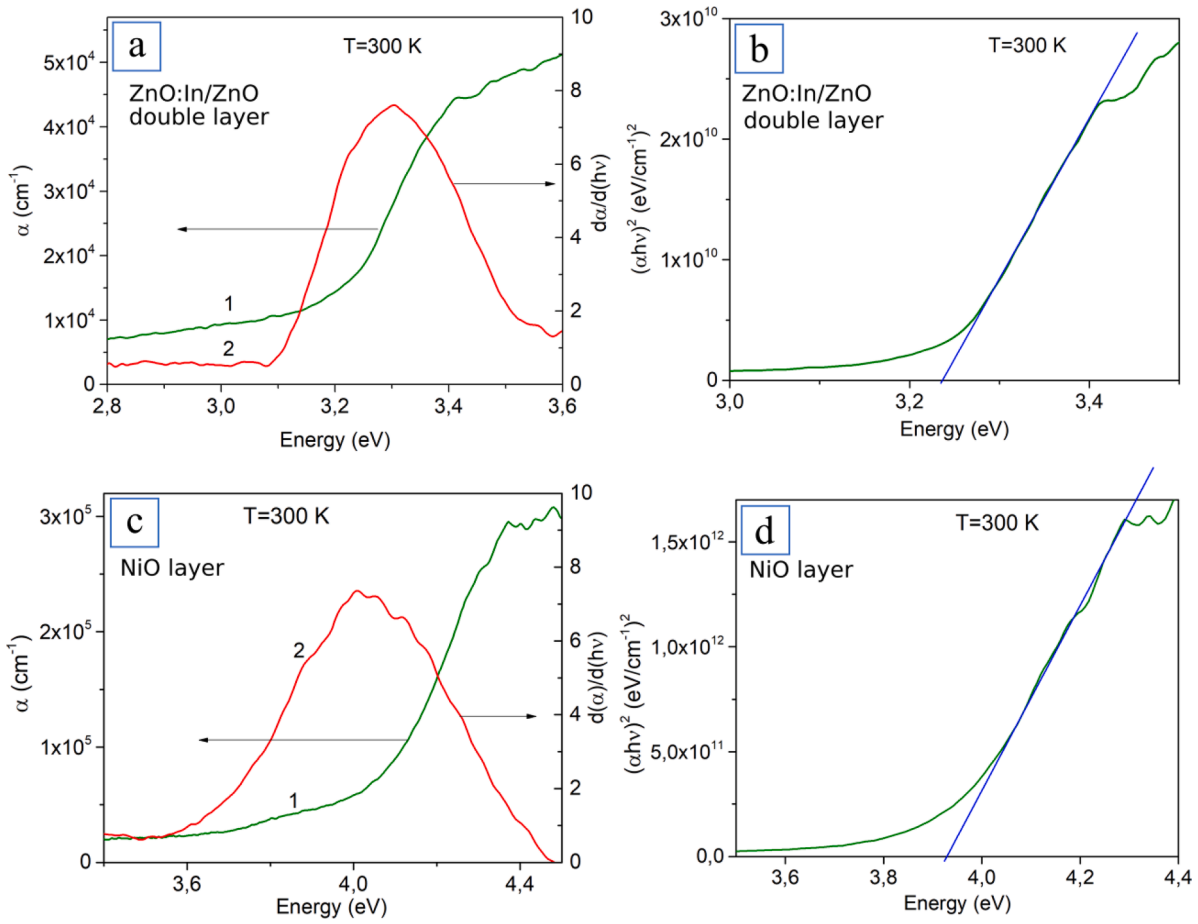

Fig. 8. (a) Absorption edge of the n-type ZnO:In/ZnO double layer of the ITO/ZnO:In/ZnO/NiO heterostructure (curve 1) and determination of its band gap by the ACFD method (curve 2). (b) Tauc's approximation of the absorption edge of ZnO:In/ZnO double layer. (c) The absorption edge of the p-type NiO layer of the ITO/ZnO:In/ZnO/NiO heterostructure (curve 1) and determination of its band gap by the ACFD method (curve 2). (d) Absorption edge approximation of the NiO layer by Tauc. The results correspond to the samples annealed at T_a = 350 °C.

Table 2
The band gaps of the ZnO:In/ZnO double and NiO layers of the ITO/ZnO:In/ZnO/NiO heterostructure in the case of the unannealed sample and samples annealed at different temperatures.

T, ° *C*	Unannealed	300	350	400	450	500
ZnO:In /ZnO						
E_g, eV ACFD	3.30	3.30	3.30	3.29	3.30	3.30
E_g, eV Tauc	3.23	3.22	3.22	3.22	3.23	3.20
NiO						
E_g, eV ACFD	4.02	4.05	4.04	4.04	4.06	4.05
E_g, eV Tauc	3.91	3.94	3.92	3.94	3.94	3.94

sample annealed at T_a = 300 °C. Here, two PL bands at 488 (2.54 eV) and 529 nm (2.34 eV) are also observed in the case of the NiO layer. At the same time, the broad PL band at 745 nm is considerably smaller in intensity (curve 1) in comparison with the intensity of this band in the case of the excitation of the NiO layer (curve 2). Similar PL spectra were also obtained in the case of the sample annealed at 450 °C, where the emission of ZnO:In/ZnO layers at 745 nm is practically absent (see Fig. 9 c). It should be noted that the intensity of the PL spectrum in the spectral region from 400 to 500 nm significantly decreases in the case of excitation of the NiO layer.

As can be seen from Fig. 9 d, in the case of the sample annealed at 500 °C, the intensity of the PL spectra in the short-wavelength region (400 – 600) nm is considerably smaller in comparison with the intensity of the PL band at 745 nm. So, the obtained results of the study of the structure of PL spectra of ZnO:In/ZnO and NiO layers allow us to obtain information about the defective structure and optical quality of these layers of the studied heterostructures and changes in these characteristics as a result of their thermal annealing. In particular, it was shown that annealing of the Glass/ITO/ZnO:In/ZnO/NiO heterostructure at $T_a \geq$ 300 °C leads to the fact that the PL band at 745 nm significantly decreases in intensity and almost does not appear in the PL spectrum of the ZnO:In/ZnO layers. This indicates a significant decreasing, probably, of antisite defects as a result of the annealing of the heterostructure at this temperature. A strong decrease in the intensity of photoluminescence in the spectral region of (400 – 600) nm in the case of zinc oxide layers is associated with the presence of a notable deterioration of the crystal structure of the layers at such annealing temperature (for T_a = 500 °C).

3.5. *Photoconductivity spectra*

Fig. 10 shows the photoconductivity spectrum of an as-deposited Glass/ITO/ZnO:In/ZnO/NiO heterostructure, i.e in the case of an unannealed sample. A number of narrow lines at 304.4 (4.07 eV), 313.4 (3.96 eV), 326.4 (3.80 eV), and 346.5 (3.58 eV) nm are observed in the short-wavelength spectral region. The last line corresponds to band-to-band transitions of ZnO layers [39]. Another shorter-wavelength line corresponds to similar photo transitions associated with the NiO layer [31]. Therefore, the band gaps of the ZnO and NiO layers correspond to energies of 3.58 and 4.07 eV, respectively. The value of E_g of NiO practically coincides with the value obtained from the approximation of

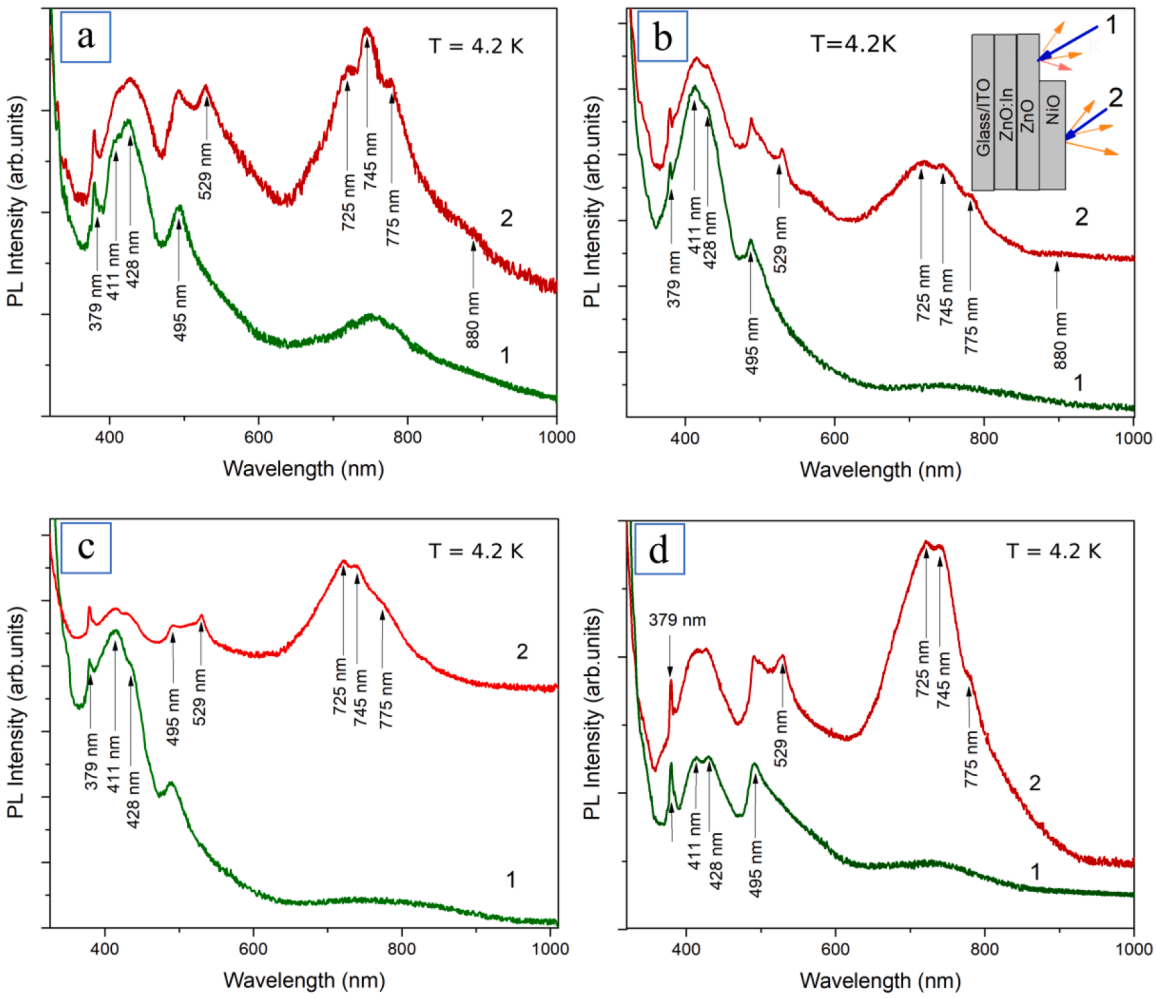

Fig. 9. Low-temperature (4.2 K) PL spectra of the *n*-type ZnO:In/ZnO double layer of the ITO/ZnO:In/ZnO/NiO heterostructure (curve 1) and *p*-type NiO layer of the ITO/ZnO:In/ZnO/NiO heterostructure (curve 2), respectively, in the case of unannealed (a) and annealed at 300 (b), 450 (c) and 500° C (d) samples. The scheme of such measurements is shown in the inset of Fig. 9 b.

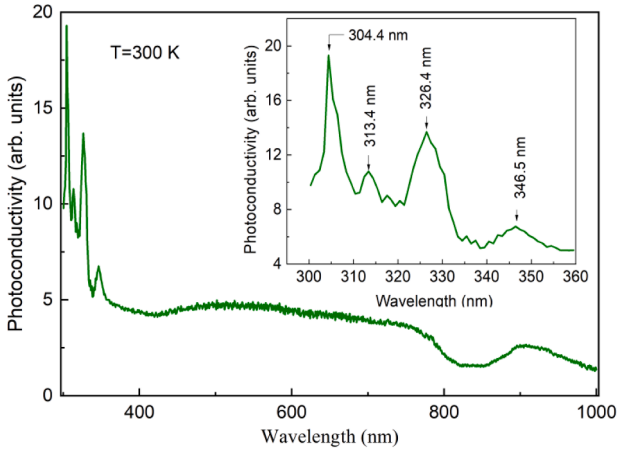

Fig. 10. Photoconductivity spectrum of the Glass/ITO/ZnO:In/ZnO/NiO heterostructure of the unannealed sample.

the absorption edge using the ACFD method. The absorption plateau in the wide spectral range from 400 to 800 nm is associated with the presence of defects in both ZnO and NiO layers.

The photoconductivity spectrum of the sample annealed at 300 °C is shown in Fig. 11 a. In this spectrum, a series of relatively narrow lines are observed at 326.4 (3.799 eV), 358.5 (3.459 eV), 383.5 (3.233 eV), and 437.6 (2.834 eV) nm. The last line is due to the presence of donor centers in ZnO associated with the presence of interstitial zinc atoms [40]. The lines at 358.5 (3.459 eV) and 383.5 (3.234 eV) can be attributed to the dissociation of free and bound excitons in ZnO [39]. While the shortest-wavelength line at 326.4 (3.799 eV) could be due to the dissociation of free or bound excitons in NiO since the binding energy of excitons in this compound is 110 meV [49]. In the long-wavelength region of the spectrum, a broad band is observed, covering a wide spectral range from 600 nm to 1000 nm. This band has a number of features at the long- and short-wavelength absorption edges at 740 (1.67 eV) and 930 nm (1.33 eV). The origin of the band at 740 nm is has been related to the presence of the O_{Zn} antisite defect [43]. The nature of the broad band at 840 nm (1.47 eV) is unknown and requires further study out of the scope of this work. Nevertheless, it is clear that this band should be due to the presence of structural defects in ZnO or NiO. It should be noted that the nature of these absorption bands is apparently similar to the PL bands at 745 and 870 nm observed in the unannealed sample.

Fig. 11 b shows the photoconductivity spectrum of the heterostructure annealed at the temperature of 350 °C. The spectrum presents a series of lines in the short-wavelength region at 322 nm (3.850 eV), 341 nm (3.637 eV), 400 nm (3.100 eV), and 450 nm (2.755 eV). The first two lines can be associated with the dissociation of free and bound

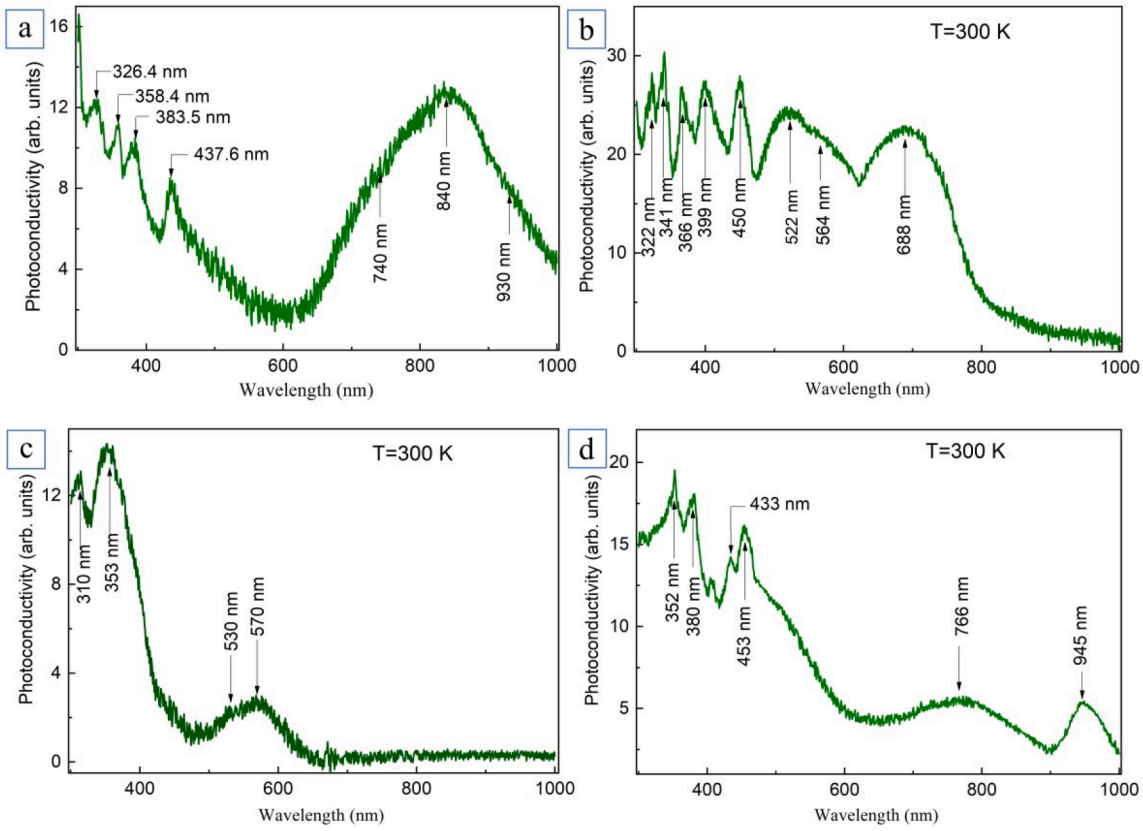

Fig. 11. Photoconductivity spectra of the Glass/ITO/ZnO:In/ZnO/NiO heterostructures of the samples annealed at T_a = 300 (a), 350 (b) 450 (c) 500 (d) ^{o}C.

excitons in NiO nanoparticles [50]. The line at 366 nm belongs to ZnO. Another line at 450 nm (2.755 eV) is associated with the presence of donor centers in ZnO [39,40]. In addition, broad bands at 522 nm (2.375 eV), 564 nm (2.199 eV) and 688 nm (1.802 eV) can be seen in the spectrum. The first band could be due to the participation of the deep V_O^{2+} zinc vacancy level and a shallow donor level [39]. The band at 564 nm (2.199 eV) is associated with oxygen vacancies in ZnO [39]. While the broad band at 688 nm (1.802 eV) is related to the antistructural defect of O_{Zn} [42,43].

Fig. 11c shows the photoconductivity spectrum of the Glass/ITO/ZnO:In/ZnO/NiO heterostructure annealed at T_a = 400 ^{o}C. As can be seen, two bands in the ultraviolet region of the spectrum at 312 nm (3.97 eV) and 353 nm (3.51 eV) appear, which are associated with band-to-band transitions of NiO and ZnO, respectively[31–34,48]. The broad band at 570 nm (2.17 eV) is caused by the presence of antisite defects [42,43]. At the short wavelength edge of this band, a kink is visible at 570 nm (2.17 eV), which, as already mentioned, is caused by oxygen vacancies in NiO [51]. It should be noted that the intensity of these bands is non-significant and that other bands are not present in the spectrum. This indicates the positive effect of annealing on the optical and crystalline quality of the investigated heterostructures.

Fig. 11d shows the photoconductivity spectrum of the Glass/ITO/ZnO:In/ZnO/NiO heterostructure annealed at T_a = 500 ^{o}C. Now the two bands in the ultraviolet region of the spectrum are located at 352 nm (3.52 eV) and 380 nm (3.26 eV), being associated with the dissociation of excitons in the zinc oxide layers [51]. The other two bands at 433 nm (2.86 eV) and 453 nm (2.74 eV) correspond to a shallow donor level and zinc vacancies [40]. The bands at 766 nm (1.62 eV) and 945 nm (1.31 eV) correspond to phototransitions involving deep levels of different structural defects.

3.6. Volt-ampere characteristics

The dark I-V characteristics of the obtained multilayer structures were measured by using a similar procedure as in ref [1] at temperatures between 30 and 80 °C with steps of 10 °. It was found that the corresponding dependencies for unannealed and annealed at low-temperature heterostructures (< 400 °C) were linear. However, the IVs became nonlinear at the annealing temperature T_a = (400 – 450) °C. The corresponding curves of *n*-ZnO/*p*-NiO heterostructures annealed at T_a = 450 °C are shown in Fig. 12 a. The rectification coefficient of the obtained structures did not exceed 3.5 (at 1 V), and the contact potential difference was (0.71–0.76) V. Similar results for the contact voltage U_k = (0.71–0.77) V were obtained in [52]. The series resistance of such structures was 335 Ohm.

To explain current transport through heterostructures that are far from ideal, the Van Ruyven model is usually used [53], which considers the presence of a layer of matter with a distorted crystal lattice and a high rate of charge carrier recombination at the interfacial boundary. Accordingly, electrons and holes reach the surface states at this boundary by tunneling from the energy bands of the materials, forming the heterostructure.

The estimation of the density of interfacial states carried out in [1] indicates that at the *n*-ZnO/*p*-NiO heterostructure boundary, dislocations of mismatch with the density of $N_s = (8.2 - 14.9) \cdot 10^{14} \cdot$ cm^{-2} can occur, in which the recombination of charge carriers occurs during charge transfer. This value is much higher than the values characteristic of heterostructures, which are close to ideal. Therefore, we used the approximation proposed for nonthermal current transfer mechanisms [54] to analyze the I-V behavior.

$$J = J_0[\exp(\pm\alpha U) - 1], J_0 = J_{00}\exp(\beta T) \quad (3)$$

where J_{00}, α, β are constants that do not depend on U and T.

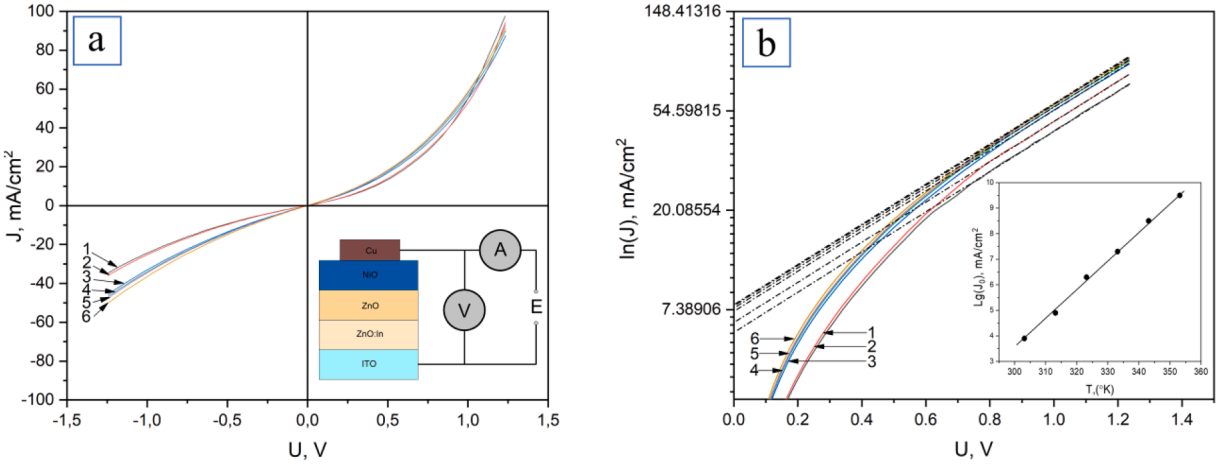

Fig. 12. Dark I-V characteristics of *n*-ZnO/*p*-NiO heterojunctions annealed at a temperature of T_a = 450 °C (a), straight branches of I-V characteristics in a semi-logarithmic scale (b). The dependences were measured in air at a temperature of 30 (1), 40 (2), 50 (3), 60 (4), 70 (5), 80 (6) °C. The inset shows the temperature dependence of current J_0 (equation (6)).

It is easy to see that the function describing the I-V is linear in the coordinates ln$J$ – U. The slope of the line in the case of nonthermal currents does not depend on the temperature of the I-V(T) measurement. The intersection of this line with the ordinate axis allowed us to determine the current density J_0, and the slope was constant α (Fig. 12 b). Accordingly, the construction of the dependence of $J_0 - T$ allows us to determine the constant β using the angle of its slope to the temperature axis. The corresponding dependencies required for the calculations are shown in Fig. 12 b and its inset. The obtained values of the constants were equal to $\alpha = 1.16\ 10^{-4}\ V^{-1}$, $\beta = 2.051\ K^{-1}$. Unfortunately, these values are not usually present in the current literature, so no comparison is possible.

4. Summary and conclusions

In this work, the effect of annealing on the optical, photoelectric and I/V electrical properties of *n*-ZnO/*p*-NiO heterostructures deposited by spray pyrolysis was studied. Analysis of the X- ray diffractograms showed that only the hexagonal phase of the ZnO and the cubic phase of NiO are present in the layers of the heterostructure. This was also confirmed by Raman spectroscopy.

The structural properties of the ZnO and NiO layers were calculated based on the positions of the X-ray diffraction peaks. It can be seen that the lattice parameters of the ZnO layer begin to increase rapidly at an annealing temperature of more than 400 °C and reach the values a = (0.3262–0.3262) nm and c = (0.5223–0.5224) nm at T_a = 500 °C. The lattice parameter of the nickel oxide layer, in turn, begins to increase at an annealing temperature of 350 °C and reaches the value of a = (0.4204–0.4201) nm at the maximum annealing temperature.

The analysis of PL spectra made it possible to investigate the defect structure and optical quality of individual ZnO:In/ZnO and NiO layers as a function of the annealing temperature. It was established that the annealing of the ITO/ZnO:In/ZnO/NiO heterostructure at $T_a \geq 300$ °C leads to a significant decrease in the intensity of the PL band at 745 nm, which is caused by a strong decrease in the O_{Zn} antisite defects in the heterostructures and an improvement in their optical quality.

The photoconductivity spectra were also used to determine the band gap of the materials, the values of which correlated well with the values obtained by the ACFD method. It was shown that the photoconductivity spectra contain lines related to the dissociation of free and bound excitons in the ZnO and NiO nanocrystallites. In addition, other bands are associated with the presence of structural defects are also observed. It should be noted that the intensity of these bands was low. This confirms the high optical and crystalline quality of the oxide layers in the studied heterostructures.

For the *n*-ZnO/*p*-NiO heterostructure annealed at T_a = 450 °C, dark I-V curves were measured at different temperatures. The construction of straight branches of the dark I-V characteristics of the obtained heterostructures on a semi-logarithmic scale showed that the charge transfer in the heterostructure was determined by the tunneling-recombination mechanism with constants$\alpha = 1{,}16\ 10^{-4}\ V^{-1}$ and $\beta = 2051\ K^{-1}$.

Thus, the obtained results indicate that the use of temperature annealing made it possible to determine the optimal conditions for *n*-ZnO/*p*-NiO heterostructure - 450 °C. This temperature provided the best properties of the heterostructure deposited by the simple, cheap and scalable spray pyrolysis method. It should be noted that temperature annealing of the studied samples belongs to the traditional methods of changing the crystalline quality.

Based on these results we would like to open new paths in order to deepen into the analysis of the obtained heterostructure by using a simple and scalable technique, like studies involving alternative doping or treatment methods, such as chemical treatments or laser irradiation, to compare the efficiency of these methods in modifying the optical and electrical properties of the heterostructures. As well as to perform detailed characterization of defects, which will improve the understanding of defect-related optical transitions; investigation of structural changes above 500 °C to gain a more complete picture of the limits of thermal stability and material integrity, which are critical for potential real-world applications; the use of deep-level transient spectroscopy (DLTS), to improve defect characterization and increase predictive power for future device performance improvements; the development of $Zn_xNi_{1-x}O$ buffer layers by long-term annealing in order to reconcile the mismatch of constants and types of the crystal lattice of ZnO and NiO compounds to improve electrical properties and increase the efficiency of the *n*-ZnO/*p*-NiO heterojunction.

CRediT authorship contribution statement

M. Yermakov: Writing – review & editing, Writing – original draft, Project administration, Formal analysis, Conceptualization. **R. Pshenychnyi:** Methodology, Formal analysis, Data curation. **A. Opanasyuk:** Writing – original draft, Validation, Supervision, Methodology. **Yu. Gnatenko:** Writing – review & editing, Validation, Methodology, Formal analysis. **P. Bukivskij:** Methodology, Data curation. **A. Bukivskii:** Formal analysis, Data curation. **O. Klymov:** Writing – review & editing, Validation, Investigation. **V. Muñoz-Sanjosé:** Writing – review & editing, Validation, Supervision, Formal analysis. **R. Gamernyk:** Formal analysis, Data curation.

Declaration of competing interest

The authors declare that they have no known competing financial interests or personal relationships that could have appeared to influence the work reported in this paper.

Acknowledgements

The work was supported by the NATO under program "Science for Peace and Security" (project SPS MYR.G5916), Ministry of Education and Science of Ukraine (0122U000787 and 0121U112687), the National Academy of Sciences of Ukraine (grant number: 1.4. B/217), Spanish Ministry of Science and Innovation/AEI under Project PID2020–114796RB-C22 (PROYECTO/AEI/10.13039/501100011033), and the Generalitat Valenciana under Project PROMETEU/2021/066. The authors also want to acknowledge access to the Servei Central de Suport a la Investigación Experimental (SCSIE) at the University of Valencia.

Data availability

Data will be made available on request.

References

[1] M. Yermakov, R. Pshenychnyi, A. Opanasyuk, O. Klymov, V. Muñoz-Sanjosé, Optical and electrical properties of ZnO/NiO heterojunctions obtained by the spray-pyrolysis method, J. Mater. Sci. (2024), https://doi.org/10.1007/s10853-024-10110-y.

[2] J. Huang, B. Li, Y. Hu, X. Zhou, Z. Zhang, Y. Ma, K. Tang, L. Wang, Y. Lu, Transparent *p*-NiO/*n*-ZnO heterojunction ultraviolet photodetectors prepared on flexible substrates, Surf. Coat. Technol. 362 (2019) 57–61, https://doi.org/10.1016/j.surfcoat.2019.01.099.

[3] R. Karsthof, H. von Wenckstern, J. Zúñiga-Pérez, C. Deparis, M. Grundmann, Nickel oxide–based heterostructures with large band offsets, Phys. Status Solidi (b) (2020) 257, https://doi.org/10.1002/pssb.201900639.

[4] Y. Liu, G. Li, R. Mi, C. Deng, P. Gao, An environment-benign method for the synthesis of *p*-NiO/*n*-ZnO heterostructure with excellent performance for gas sensing and photocatalysis, Sens. Actuators. B Chem. 191 (2014) 537–544, https://doi.org/10.1016/j.snb.2013.10.068.

[5] A.M.A. Majeed, A.D. Nusseif, N.S. Hameed, Investigations of ZnO-NiO/*p*-Si heterojunction for solar cell application, in: 2019: p. 030015. 10.1063/1.5123085.

[6] G. Vijaya Prasath, K.S. Usha, M. Karuppaiah, G. Ravi, P. Krishnan, Fabrication of heterostructure NiO/ZnO thin film for pseudocapacitor application, J. Solgel Sci. Technol. 104 (2022) 198–210, https://doi.org/10.1007/s10971-022-05919-5.

[7] N.P. Klochko, V.R. Kopach, I.I. Tyukhov, D.O. Zhadan, K.S. Klepikova, G. S. Khrypunov, S.I. Petrushenko, V.M. Lyubov, M.V. Kirichenko, S.V. Dukarov, A. L. Khrypunova, Metal oxide heterojunction (NiO/ZnO) prepared by low temperature solution growth for UV-photodetector and semi-transparent solar cell, Sol. Energy 164 (2018) 149–159, https://doi.org/10.1016/j.solener.2018.01.054.

[8] H. Hakkoum, A. Moumen, M. Ghougali, N. Sengouga, E. Comini, The effect of structural characteristics of ZnO and NiO thin films on the performance of NiO/ZnO photodetectors, J. Mater. Sci. Mater. Electron. 33 (2022) 26604–26618, https://doi.org/10.1007/s10854-022-09336-w.

[9] Y. Chen, Review of ZnO transparent conducting oxides for solar applications, IOP Conf. Ser. Mater. Sci. Eng. 423 (2018) 012170, https://doi.org/10.1088/1757-899X/423/1/012170.

[10] M.A. Borysiewicz, ZnO as a functional material, a review, Crystals 9 (2019) 505, https://doi.org/10.3390/cryst9100505 (Basel).

[11] T.H. Chuang, C.K. Wen, S.C. Chen, M.H. Liao, F. Liu, H. Sun, p-type semi-transparent conductive NiO films with high deposition rate produced by superimposed high power impulse magnetron sputtering, Ceram. Int. 46 (2020) 27695–27701, https://doi.org/10.1016/j.ceramint.2020.07.267.

[12] P. Salunkhe, M.A. AV, D. Kekuda, Investigation on tailoring physical properties of Nickel Oxide thin films grown by dc magnetron sputtering, Mater. Res. Express. 7 (2020) 016427, https://doi.org/10.1088/2053-1591/ab69c5.

[13] P.K. Salokhe, S.S. Shetti, V.D. Patil, T.R. Patil, R.M. Nille, A.B. Chougale, K. T. Gurav, R.B. Sutar, A.A. Jatratkar, G.G. Chougale, J.B. Yadav, B.M. Mohite, S. M. Bargir, R.B. Patil, S.H. Tamboli, Study of physical properties of chemical bath deposited nickel oxide thin films, Mater. Today Proc. 43 (2021) 2810–2813, https://doi.org/10.1016/j.matpr.2020.09.328.

[14] D.S. Dalavi, N.S. Harale, I.S. Mulla, V.K. Rao, V.B. Patil, I.Y. Kim, J.H. Kim, P. S. Patil, Nanoporous network of nickel oxide for ammonia gas detection, Mater. Lett. 146 (2015) 103–107, https://doi.org/10.1016/j.matlet.2015.01.138.

[15] M. Napari, T.N. Huq, R.L.Z. Hoye, J.L. MacManus-Driscoll, Nickel oxide thin films grown by chemical deposition techniques: Potential and challenges in next-generation rigid and flexible device applications, InfoMat 3 (2021) 536–576, https://doi.org/10.1002/inf2.12146.

[16] V. Kosyak, Y. Znamenshchykov, A. Čerškus, Y.P. Gnatenko, L. Grase, J. Vecstaudza, A. Medvids, A. Opanasyuk, G. Mezinskis, Composition dependence of structural and optical properties of $Cd_{1-x}Zn_xTe$ thick films obtained by the close-spaced sublimation, J. Alloys. Compd. 682 (2016) 543–551, https://doi.org/10.1016/j.jallcom.2016.05.065.

[17] A.A. Akl, I.M. El Radaf, A.S. Hassanien, An extensive comparative study for microstructural properties and crystal imperfections of Novel sprayed Cu3SbSe3 Nanoparticle-thin films of different thicknesses, Optik 227 (2021) 165837, https://doi.org/10.1016/j.ijleo.2020.165837 (Stuttg).

[18] O. Dobrozhan, S. Vorobiov, D. Kurbatov, M. Baláž, M. Kolesnyk, O. Diachenko, V. Komanicky, A. Opanasyuk, Structural properties and chemical composition of ZnO films deposited onto flexible substrates by spraying polyol mediated nanoinks, Superlattices Microstruct. 140 (2020) 106455, https://doi.org/10.1016/j.spmi.2020.106455.

[19] S. Kakherskyi, R. Pshenychnyi, O. Dobrozhan, Ja.G. Vaziev, A.P. Bukivskii, P. M. Bukivskij, Yu.P. Gnatenko, A. Opanasyuk, Structural, microstructural, chemical, and optical properties of NiO nanocrystals and films obtained by 3D printing, Appl. Phys. A 127 (2021) 715, https://doi.org/10.1007/s00339-021-04847-5.

[20] R. Raciti, R. Bahariqushchi, C. Summonte, A. Aydinli, A. Terrasi, S. Mirabella, Optical bandgap of semiconductor nanostructures: methods for experimental data analysis, J. Appl. Phys. 121 (2017), https://doi.org/10.1063/1.4986436.

[21] B. Ullrich, G.J. Brown, H. Xi, Semiconductor band gap localization via Gaussian function, Semicond. Sci. Technol. 27 (2012) 105016, https://doi.org/10.1088/0268-1242/27/10/105016.

[22] J. Tamayo-Arriola, A. Huerta-Barberà, M. Montes Bajo, E. Muñoz, V. Muñoz-Sanjosé, A. Hierro, Rock-salt CdZnO as a transparent conductive oxide, Appl. Phys. Lett. 113 (2018), https://doi.org/10.1063/1.5048771.

[23] B. Son, Y. Lin, K.H. Lee, Q. Chen, C.S. Tan, Dark current analysis of germanium-on-insulator vertical *p-i-n* photodetectors with varying threading dislocation density, J. Appl. Phys. 127 (2020), https://doi.org/10.1063/5.0005112.

[24] R. Cuscó, E. Alarcón-Lladó, J. Ibáñez, L. Artús, J. Jiménez, B. Wang, M.J. Callahan, Temperature dependence of Raman scattering in ZnO, Phys. Rev. B 75 (2007) 165202, https://doi.org/10.1103/PhysRevB.75.165202.

[25] A. Bedia, F.Z. Bedia, M. Aillerie, N. Maloufi, S.Ould Saad Hamady, O. Perroud, B. Benyoucef, Optical, electrical and structural properties of nano-pyramidal ZnO films grown on glass substrate by spray pyrolysis technique, Opt. Mater. 36 (2014) 1123–1130, https://doi.org/10.1016/j.optmat.2014.02.012 (Amst).

[26] D. Behera, B.S. Acharya, Nano-star formation in Al-doped ZnO thin film deposited by dip-dry method and its characterization using atomic force microscopy, electron probe microscopy, photoluminescence and laser Raman spectroscopy, J. Lumin. 128 (2008) 1577–1586, https://doi.org/10.1016/j.jlumin.2008.03.006.

[27] C. Mrabet, N. Mahdhi, A. Boukhachem, M. Amlouk, T. Manoubi, Effects of surface oxygen vacancies content on wettability of zinc oxide nanorods doped with lanthanum, J. Alloys. Compd. 688 (2016) 122–132, https://doi.org/10.1016/j.jallcom.2016.06.286.

[28] A. Sunny, K. Balasubramanian, Plasmon induced enhancement of surface optical phonon modes and magnon properties of NiO nanoparticles: Raman spectral probe, Phys. Chem. Chem. Phys. 22 (2020) 22815–22822, https://doi.org/10.1039/D0CP03720F.

[29] A. Sunny, K. Balasubramanian, Raman spectral probe on size-dependent surface optical phonon modes and magnon properties of NiO nanoparticles, J. Phys. Chem. C 124 (2020) 12636–12644, https://doi.org/10.1021/acs.jpcc.0c02638.

[30] A. Sunny, K. Balasubramanian, Laser-induced phonon and magnon properties of NiO nanoparticles: a Raman study, J. Raman Spectrosc. 52 (2021) 833–842, https://doi.org/10.1002/jrs.6067.

[31] R.J. Powell, W.E. Spicer, Optical properties of NiO and CoO, Phys. Rev. B 2 (1970) 2182–2193, https://doi.org/10.1103/PhysRevB.2.2182.

[32] K. Anandan, V. Rajendran, Morphological and size effects of NiO nanoparticles via solvothermal process and their optical properties, Mater. Sci. Semicond. Process. 14 (2011) 43–47, https://doi.org/10.1016/j.mssp.2011.01.001.

[33] Z.N. Kayani, M.Z. Butt, S. Riaz, S. Naseem, Synthesis of NiO nanoparticles by sol-gel technique, Mater. Sci. 36 (2018) 547–552, https://doi.org/10.2478/msp-2018-0088. Poland.

[34] J. Tauc, Optical properties and electronic structure of amorphous Ge and Si, Mater. Res. Bull. 3 (1968) 37–46, https://doi.org/10.1016/0025-5408(68)90023-8.

[35] W.Z. Shen, A novel approach for the evaluation of band gap energy in semiconductors, J. Infrared Millim. Waves 23 (2002) 61–69, https://doi.org/10.1023/A:1015033901163.

[36] Yu.P. Gnatenko, P.M. Bukivskij, R.V. Gamernyk, V.Yu. Yevdokymenko, A. S. Opanasyuk, A.P. Bukivskii, M.S. Furyer, L.M. Tarakhan, Study of optical and photoelectric properties of copper oxide films, Mater. Chem. Phys. 307 (2023) 128175, https://doi.org/10.1016/j.matchemphys.2023.128175.

[37] Yu.P. Gnatenko, P.M. Bukivskij, A.S. Opanasyuk, D.I. Kurbatov, M.M. Kolesnyk, V. V. Kosyak, H. Khlyap, Low-temperature photoluminescence of II-VI films obtained by close-spaced vacuum sublimation, J. Lumin. 132 (2012) 2885–2888, https://doi.org/10.1016/j.jlumin.2012.06.003.

[38] V.Yu. Yevdokymenko, O. Dobrozhan, R. Pshenychnyi, A. Opanasyuk, Yu. Gnatenko, A. Bukivskii, P. Bukivskij, R. Gamernyk, O. Klymov, V. Muñoz-Sanjosé, P. Ibañez-Romero, Z. Gacevic, The effect of annealing treatment on the structural and optical properties of nanostructured Cu_xO films obtained by 3D printing, Mater. Sci. Semicond. Process. 161 (2023) 107472, https://doi.org/10.1016/j.mssp.2023.107472.

[39] A. Teke, Ü. Özgür, S. Doğan, X. Gu, H. Morkoç, B. Nemeth, J. Nause, H.O. Everitt, Excitonic fine structure and recombination dynamics in single-crystalline ZnO, Phys. Rev. B 70 (2004) 195207, https://doi.org/10.1103/PhysRevB.70.195207.

[40] M.D. McCluskey, S.J. Jokela, Defects in ZnO, J. Appl. Phys. 106 (2009), https://doi.org/10.1063/1.3216464.
[41] M. Willander, O. Nur, J.R. Sadaf, M.I. Qadir, S. Zaman, A. Zainelabdin, N. Bano, I. Hussain, Luminescence from zinc oxide nanostructures and polymers and their hybrid devices, Materials 3 (2010) 2643–2667, https://doi.org/10.3390/ma3042643.
[42] T. Ganesh, K. Perumal, R. Kumar, N. Bhaskar, Effect of thickness on microstructural and optical properties of Al-doped ZnO films prepared by sol-gel spin coating, Nano Hybrids and Compos. 17 (2017) 171–178, https://doi.org/10.4028/www.scientific.net/NHC.17.171.
[43] A. Janotti, C.G. Van de Walle, Native point defects in ZnO, Phys. Rev. B 76 (2007) 165202, https://doi.org/10.1103/PhysRevB.76.165202.
[44] A. Gandhi, S. Wu, Strong deep-level-emission photoluminescence in NiO nanoparticles, Nanomaterials 7 (2017) 231, https://doi.org/10.3390/nano7080231.
[45] D.Y. Jiang, J.M. Qin, X. Wang, S. Gao, Q.C. Liang, J.X. Zhao, Optical properties of NiO thin films fabricated by electron beam evaporation, Vacuum 86 (2012) 1083–1086, https://doi.org/10.1016/j.vacuum.2011.10.003.
[46] G. Madhu, V. Biju, Effect of Ni^{2+} and O^{2-} vacancies on the electrical and optical properties of nanostructured nickel oxide synthesized through a facile chemical route, Phys. E Low-Dimens. Syst. Nanostructures 60 (2014) 200–205, https://doi.org/10.1016/j.physe.2014.02.011.
[47] A.H. Hammad, M.Sh. Abdel-wahab, S. Vattamkandathil, A.R. Ansari, Influence the oxygen flow rate on the film thickness, structural, optical and photoluminescence behavior of DC sputtered NiO thin films, Phys. B Condens. Matter. 568 (2019) 6–12, https://doi.org/10.1016/j.physb.2019.05.012.
[48] M.K. Debanath, S. Karmakar, Study of blueshift of optical band gap in zinc oxide (ZnO) nanoparticles prepared by low-temperature wet chemical method, Mater. Lett. 111 (2013) 116–119, https://doi.org/10.1016/j.matlet.2013.08.069.
[49] M. Patel, H.S. Kim, J. Kim, J.H. Yun, S.J. Kim, E.H. Choi, H.H. Park, Excitonic metal oxide heterojunction (NiO/ZnO) solar cells for all-transparent module integration, Sol. Energy Mater. Sol. Cells 170 (2017) 246–253, https://doi.org/10.1016/j.solmat.2017.06.006.
[50] C.H. Ho, Y.M. Kuo, C.H. Chan, Y.R. Ma, Optical characterization of strong UV luminescence emitted from the excitonic edge of nickel oxide nanotowers, Sci. Rep. 5 (2015) 15856, https://doi.org/10.1038/srep15856.
[51] J. Petersen, F. Twagirayezu, P.D. Borges, L. Scolfaro, W. Geerts, Ab initio study of oxygen vacancy effects on electronic and optical properties of NiO, MRS Adv. 1 (2016) 2617–2622, https://doi.org/10.1557/adv.2016.405.
[52] M. Patel, H.S. Kim, J. Kim, J.H. Yun, S.J. Kim, E.H. Choi, H.H. Park, Excitonic metal oxide heterojunction (NiO/ZnO) solar cells for all-transparent module integration, Sol. Energy Mater. Sol. Cells 170 (2017) 246–253, https://doi.org/10.1016/j.solmat.2017.06.006.
[53] L.J. van Ruyven, The position of the fermi level at a hetero-junction interface, Phys. Status Solidi (b) 5 (1964), https://doi.org/10.1002/pssb.19640050326.
[54] A.S. Opanasyuk, D.I. Kurbatov, M.M. Ivashchenko, I.Y. Protsenko, H. Cheong, Properties of the window layers for the CZTSe and CZTS based solar cells, J. Nano Electron. Phys. 4 (2012) 01024.